

Majorana Doublets, Flat Bands, and Dirac Nodes in s -Wave Superfluids

Haiping Hu, Fan Zhang, and Chuanwei Zhang*

Department of Physics, The University of Texas at Dallas, Richardson, Texas 75080, USA

Topological superfluids protected by mirror and time-reversal symmetries are exotic states of matter possessing Majorana Kramers pairs (MKPs), yet their realizations have long been hindered by the requirement of unconventional pairing. We propose to realize such a topological superfluid by utilizing s -wave pairing and emergent mirror and time-reversal symmetries in two coupled 1D ultracold atomic Fermi gases with spin-orbit coupling. By stacking such systems into 2D, we discover topological and Dirac-nodal superfluids hosting distinct MKP flat bands. We show that the emergent symmetries make the MKPs and their flat bands stable against pairing fluctuations that otherwise annihilate paired Majoranas. Exploiting new experimental developments, our scheme provides a unique platform for exploring MKPs and their applications in quantum computation.

Introduction.—Spin-orbit coupling (SOC) plays a crucial role in many topological quantum phenomena of condensed matter physics [1, 2]. In ultracold atomic gases, SOC has been experimentally realized by coupling different hyperfine ground states through counter-propagating Raman lasers [3–13]. Due to their highly controllability and free of disorder, the spin-orbit coupled ultracold atomic gases have opened a broad avenue for exploring novel topological quantum matter. In particular, the cooperation of three key ingredients, i.e., SOC, Zeeman coupling, and s -wave pairing interaction, can produce effective p -wave superfluids [14–16] that host Majorana excitations [17–19]. Because of their non-Abelian braiding statistics and potential applications in fault-tolerant quantum computing [20], topological defects containing unpaired Majoranas have been extensively studied in solid-state systems nowadays [21–37].

These superfluids with unpaired Majoranas belong to class D in the ten-fold way of Altland-Zirnbauer classification [38, 39]. Without additional symmetries, the coupling between two Majoranas can lift their zero-energy degeneracy. Time-reversal (TR) symmetry ($\mathcal{T}^2 = -1$) can, however, dictate them to form a Kramers doublet, dubbed Majorana Kramers pair (MKP) [40–43]. Topological superfluids hosting protected MKPs belong to a completely distinct symmetry class, i.e., the DIII or mirror class [42]. Intriguingly, MKPs enjoy symmetry-protected non-Abelian braiding statistics [44, 45], which may constitute advantages for quantum computing.

There have been several tantalizing proposals for realizing topological superconductors hosting MKPs in solid-state materials [40–58], such as those proximitized devices exploiting the unconventional s_{\pm} -wave [41, 58], $d_{x^2-y^2}$ -wave [43], or spatially sign-switching pairing [21]. However, these schemes are challenging, as they strongly rely on the presence of exotic pairing and its fine control in materials [59]. In this context, ultracold atomic gases may provide a more controllable platform for exploring topological superfluids hosting MKPs [42]. In contrast to extrinsic proximity-induced superconductivity in solid-state platforms, superfluid orders in ultracold atomic gases are formed through intrinsic s -wave attrac-

tive interactions. In particular, a superfluid phase may be destroyed by quantum fluctuations in a 1D chain, therefore it is crucial to exploit weakly-coupled 1D chains or 2D/3D arrays to suppress quantum fluctuations. Yet, it has been shown that couplings between identical class D (and even class BDI [37]) chains induce edge pairing fluctuations that destroy Majorana modes [60, 61]. Thus, two questions naturally arise. Can TR-invariant topological mirror superfluids be realized in ultracold atomic gases with conventional s -wave pairing? If so, can TR and mirror symmetries protect MKPs from pairing fluctuations? In this Letter, we address these two important questions by showing that the remarkable physics of TR-invariant topological mirror superfluids and associated MKPs can be realized in ultracold atomic gases by utilizing experimentally accessible s -wave pairing and synthetic 1D SOC [3–10]. Here are our main findings.

First, although the Zeeman field from Raman coupling in synthetic SOC breaks TR symmetry in a Fermi gas, effective TR and mirror symmetries emerge for two coupled gases with opposite Zeeman fields (Fig. 1), which can be realized by changing the beam profile of one Raman laser from Gaussian to Hermite-Gaussian [62]. The emergent TR and mirror symmetries, together with s -wave pairing, can be exploited to realize TR-invariant topological mirror superfluids [42].

Second, by tuning the Zeeman field strength and chemical potential, our 1D system undergoes various phase transitions between different phases and the topological superfluid characterized by a \mathbb{Z}_2 invariant and the emergence of MKPs. Even though the SOC is 1D, our 2D system exhibits both topological and Dirac-nodal [63] superfluids hosting distinct flat bands of MKPs. This extension strongly suppresses quantum fluctuations that may destroy the two superfluid phases.

Thirdly, as evidenced by our self-consistent calculations [64–69], the degeneracies of MKPs and their flat bands are symmetry protected against pairing fluctuations, which are known to annihilate paired Majoranas for coupled 1D chains. (All these results also apply to the 3D case.) Therefore, our scheme provides a simple experimentally feasible route for realizing TR-invariant topo-

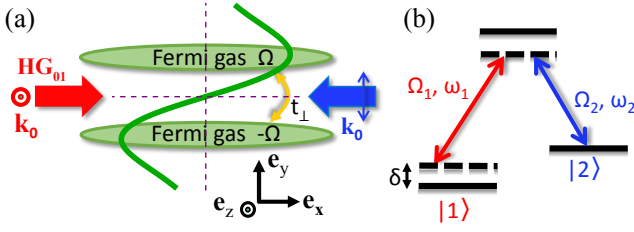


FIG. 1: Schematics of proposed experimental setups. (a) 1D SOC generated by two counter-propagating Raman lasers along \mathbf{e}_x , i.e., one HG_{01} beam (red arrow) polarized along \mathbf{e}_z with frequency ω_1 and one Gaussian beam (blue arrow) polarized along \mathbf{e}_y with frequency ω_2 . The green line shows the resulting Zeeman field along \mathbf{e}_y . (b) Two-photon process induced by the two Raman lasers in (a) with a detuning δ .

logical and Dirac-nodal superfluids, paving the way for observing MKPs and exploring their non-Abelian statistics [44, 45] and interaction effects [46, 47].

Model.—Consider two coupled 1D Fermi gases of ultracold atoms with the same SOC but opposite Zeeman fields. (A double-well trapping potential along \hat{y} is used to create this system.) As sketched in Fig. 1, the SOC can be achieved by two counter-propagating Raman lasers coupling two atomic hyperfine states $|1\rangle$ and $|2\rangle$. This setup is the same as those in previous experiments [3–13], except that one laser beam is changed from Gaussian to Hermite-Gaussian HG_{01} mode [62], and can be described by the Hamiltonian $h_k = \hbar^2 k^2 / 2m + \Omega \sigma_z + \delta \sigma_y + 2\alpha k \sigma_y$ in a rotated basis with $|1, 2\rangle = (|\uparrow\rangle \pm i|\downarrow\rangle) / \sqrt{2}$. Here k is the quasi-momentum in each gas, α is the SOC strength, δ is the two-photon detuning, and $\Omega = \Omega_0 y \exp(-y^2/w^2)$ is the position-dependent Raman coupling serving as the Zeeman field. Given the antisymmetric HG_{01} beam, the Zeeman field is opposite at the two gases, which is crucial for realizing an emergent TR symmetry.

Taking into account the s -wave interaction induced superfluidity, the physics of our 1D Fermi gas system can be described by the Bogoliubov-de Gennes (BdG) Hamiltonian [70] $H_k = \Psi_k^\dagger \mathcal{H}_k^{\text{BdG}} \Psi_k / 2$ with

$$\mathcal{H}_k^{\text{BdG}} = [\xi_k + 2\alpha \sin k \sigma_y - t_\perp s_x] \tau_z + \Omega \sigma_z s_z + \Delta \tau_x \quad (1)$$

expressed in the Nambu spinor basis $\Psi_k = (\phi_k, i\sigma_y \phi_{-k}^\dagger)$. Here $\phi_k = (c_{k\uparrow,1}, c_{k\downarrow,1}, c_{k\uparrow,2}, c_{k\downarrow,2})^T$ with $c_{k\sigma,s}$ the fermion annihilation operators; $\boldsymbol{\sigma}$, \mathbf{s} , and $\boldsymbol{\tau}$ are Pauli matrices acting on the fermion spin, *double chain*, and particle-hole spaces, respectively; $\xi_k = -2t \cos k - \mu$ is the intra-chain kinetic energy with a chemical potential μ , t_\perp is the inter-chain coupling, and $\delta = 0$ has been chosen for the detuning. The lattice regularization of the free-space fermion kinetic energy would not change any essential physics [70]. Importantly, the Zeeman field $\Omega \sigma_z s_z$ is exactly opposite for the two chains, and the s -wave pairing order parameter Δ must be self-consistently determined [64–69]. Diagonalizing the Hamiltonian (1), we

obtain the quasiparticle energy spectrum

$$E(k) = \pm \left[(2\alpha \sin k \pm t_\perp)^2 + \Omega^2 + \Delta^2 + \xi_k^2 \pm 2\sqrt{(\Delta^2 + \xi_k^2)\Omega^2 + (2\alpha \sin k \pm t_\perp)^2 \xi_k^2} \right]^{1/2}, \quad (2)$$

with two-fold degeneracies at $k = 0$ and π due to an emergent TR symmetry, as we elaborate below.

Symmetry and invariant.—The model (1) has three *independent* symmetries that govern the underlying physics. First, there is an intrinsic particle-hole symmetry reflecting the BdG redundancy: $\mathcal{P} \mathcal{H}_k^{\text{BdG}} \mathcal{P}^{-1} = -\mathcal{H}_{-k}^{\text{BdG}}$ with $\mathcal{P} = \tau_y \sigma_y \mathcal{K}$ and \mathcal{K} the complex conjugation. Second, even though the TR symmetry is explicitly broken by the Zeeman field within each chain, Eq. (1) is still invariant under TR followed by chain inversion, i.e.,

$$\tilde{\mathcal{T}} \mathcal{H}_k^{\text{BdG}} \tilde{\mathcal{T}}^{-1} = \mathcal{H}_{-k}^{\text{BdG}}, \quad \tilde{\mathcal{T}} = i s_x \sigma_y \mathcal{K}. \quad (3)$$

Given that $\tilde{\mathcal{T}}^2 = -1$, such an emergent TR symmetry dictates the Kramers degeneracies found in the spectrum (2) at $k = 0$ and π . Note that the composite operation of \mathcal{P} and $\tilde{\mathcal{T}}$ also leads to a chiral symmetry: $\mathcal{C} \mathcal{H}_k^{\text{BdG}} \mathcal{C}^{-1} = -\mathcal{H}_k^{\text{BdG}}$ with $\mathcal{C} = \mathcal{P} \tilde{\mathcal{T}}$. Thirdly, the setup has a mirror symmetry such that the two chains are the mirror images of each other, i.e.,

$$\mathcal{M} \mathcal{H}_k^{\text{BdG}} \mathcal{M}^{-1} = \mathcal{H}_k^{\text{BdG}}, \quad \mathcal{M} = i s_x \sigma_y. \quad (4)$$

Since the mirror symmetry with $\mathcal{M}^2 = -1$ is a spatial symmetry, naturally $[\mathcal{M}, \mathcal{O}] = 0$ with $\mathcal{O} = \mathcal{P}$, $\tilde{\mathcal{T}}$ and \mathcal{C} .

In light of the above symmetry analysis, the Hamiltonian (1) belongs to both the DIII class [38, 39] and the mirror class [42] in topological classification. It follows that a \mathbb{Z}_2 index ν [70, 71] and a mirror winding number γ_m , with $\nu = \gamma_m \bmod 2$ [42], can both be used for characterizing the band topology of model (1).

We find that the transitions between topologically distinct phases occur at the phase boundary where

$$\xi_k^2 + \Delta^2 = \Omega^2, \quad 4\alpha^2 \sin^2 k = t_\perp^2. \quad (5)$$

For $t_\perp = 0$, the quasiparticle gap closes at $k = 0$, and the phase boundary reduces to that of single-chain superfluids [22, 23]. For a finite t_\perp , the quasiparticle gap closes at a finite k , and the critical Zeeman fields read

$$\Omega_\pm = [(2t\sqrt{1 - t_\perp^2/4\alpha^2} \pm \mu)^2 + \Delta^2]^{1/2}. \quad (6)$$

Applying the established formulas for ν [70, 71] and γ_m [42] to Eq. (1), we conclude that

$$\nu = \gamma_m = \begin{cases} 1 & \text{if } \Omega_- < |\Omega| < \Omega_+, \\ 0 & \text{otherwise.} \end{cases} \quad (7)$$

Our model in the nontrivial regime realizes not only a TR-invariant topological superfluid but also the first topological mirror superfluid [42] in degenerate gases.

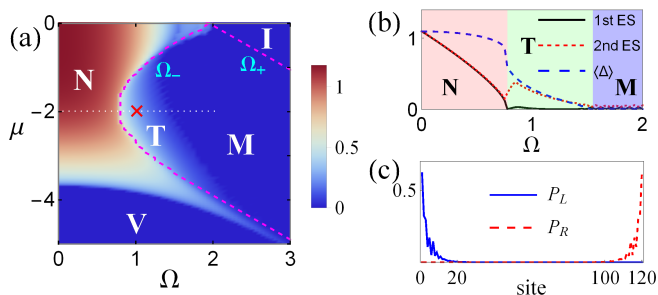


FIG. 2: (a) Phase diagram in the Ω - μ plane, symmetric with respect to $\mu = 0$ and $\Omega = 0$. The contour plot shows the site-averaged pairing $\langle \Delta \rangle$ in the normal superfluid (N), topological superfluid (T), metal with SOC (M), polarized insulator (I), and trivial vacuum (V). The dotted red lines are the phase boundaries determined by Eq. (5). (b) Phase transitions along the white dotted line in (a). The black solid (red dotted) lines denote the first (second) quasiparticle excitation states (ES) in the spectrum, both of which are two-fold degenerate. (c) Probability distributions of the left (L) and right (R) MKPs at the red cross in (a). $\sum_i P_L(i) = \sum_i P_R(i) = 2$ are the hallmarks of MKPs. $\alpha = 1$ and $t_{\perp} = 0.5$ are used in (a)-(c).

Self-consistent phase diagram.—In ultracold atomic gases, the local s -wave pair potential in real space must be determined in a self-consistent manner [64–69], together with the quasiparticle energies and wave functions. In our numerical calculations [70], the chemical potential is fixed without loss of generality, and the open boundary condition is used for the purpose of observing MKPs. We choose $L = 120$ as the length of chain, t as the energy unit, and $\langle \Delta \rangle = \sum_i |\Delta_i|/L$ as the pairing strength.

Figure 2(a) plots the phase diagram in the Ω - μ plane, which is symmetric with respect to $\mu = 0$ and $\Omega = 0$. Evidently, the numerical phase boundaries are in good harmony with those determined by Eq. (5). In total, there are five distinct phases: the normal superfluid, topological superfluid, metal with SOC, polarized insulator, and trivial vacuum. The vacuum state occurs when $|\mu|$ is too large to cross the single-particle bands. The system becomes the polarized insulator near $|\mu| = 0$ if the Zeeman field strength $|\Omega|$ is sufficiently large; each lattice site per chain is occupied by one fermion of the same polarization. At relatively smaller $|\Omega|$ and $|\mu|$, superfluidity spontaneously emerges with a finite bulk pairing gap for quasiparticle excitations. In this regime, whereas it is the normal superfluid without any boundary zero mode if both $|\Omega|$ and $|\mu|$ approach zero, it becomes the topological superfluid with two degenerate zero modes per boundary, i.e., the MKP, if $|\mu|$ approaches to the original band degeneracies and if $|\Omega| > \Omega_-$ as required in Eq. (7). As $|\Omega|$ further increases, the superfluidity gradually vanishes, and the metal phase emerges with an excitation gap scales linearly with $1/L$.

Figure 2(b) with $\mu = -2$ features the most appealing part of the phase diagram, where there are two successive

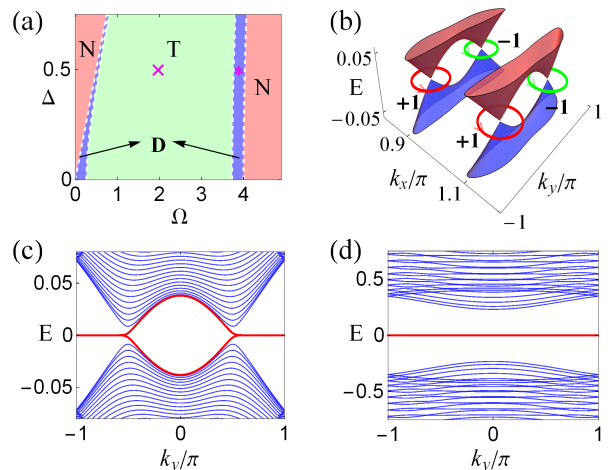


FIG. 3: (a) Phase diagram in the Ω - Δ plane for the 2D model (8). The red, green, and blue regions denote the normal (N), topological (T), and Dirac-nodal (D) superfluids, respectively. (b) Bulk quasiparticle spectrum for the Dirac superfluid labeled by the red star in (a). Each Dirac point is indexed by a winding number $\gamma_t = \pm 1$. (c)-(d) Quasiparticle spectrum with MKP edge flat bands under open boundary condition for the Dirac and topological superfluids labeled in (a). $t_1 = t_2 = 0.5$, $\alpha = 1$, and $\mu = -2$ are used in (a)-(d).

phase transitions as Ω increases from 0. The first transition occurs at $\Omega = \Omega_-$: the normal superfluid turns to the topological superfluid with the emergence of one localized MKP per boundary, as shown in Fig. 2(c). As Ω becomes stronger, the pairing strength $\langle \Delta \rangle$ becomes weaker. Eventually at the second transition, $\langle \Delta \rangle$ vanishes and the system enters into the metal phase with gapless single-particle excitations.

2D topological superfluids.—By stacking our double chains, we can obtain exotic 2D and 3D topological superfluids protected by the emergent TR and mirror symmetries. The extension to higher dimensions can suppress quantum fluctuations and stabilize long-range pairing orders. We focus on the 2D case [70], and the 3D generalization is straightforward. The staggered Zeeman field switches sign between neighboring chains along \hat{y} . This setup can be described by the BdG Hamiltonian

$$\mathcal{H}_{\mathbf{k}}^{\text{BdG}} = [\xi_{k_x} + 2\alpha \sin k_x \sigma_y - (t_1 + t_2 \cos k_y) s_x - t_2 \sin k_y s_y] \tau_z + \Omega s_z \sigma_z + \Delta \tau_x, \quad (8)$$

where t_1 and t_2 are the alternating inter-chain couplings along \hat{y} . Such a system has an emergent property

$$\tilde{\mathcal{T}} \mathcal{H}^{\text{BdG}}(k_x, k_y) \tilde{\mathcal{T}}^{-1} = \mathcal{H}^{\text{BdG}}(-k_x, k_y), \quad (9)$$

i.e., the system respects the TR symmetry in Eq. (3) and belongs to class DIII with a \mathbb{Z}_2 invariant ν_{k_y} for any k_y , which is an anomalous pumping parameter [44].

Consequently, there can be three distinct phases for Eq. (8). Whereas the superfluid is normal if $\nu_{k_y} = 0$ for

any k_y , an unprecedented topological superfluid emerges if $\nu_{k_y} = 1$ for any k_y . Remarkably in the topological phase, there emerges a flat band of MKPs at the edge along \hat{y} , because there is a MKP corresponding to the nontrivial \mathbb{Z}_2 invariant for any k_y . (This edge flat band is a consequence of the bulk topological property, and the band flatness is protected by the TR and mirror symmetries, although the edge flat band itself may be trivial [72] if treated as a 1D system.) Intriguingly, if $\nu_0 \neq \nu_\pi$, a nodal superfluid emerges. As the \mathbb{Z}_2 invariant changes from $k_y = 0$ to $k_y = \pi$, the bulk gap must close at at least one k_y in between 0 and π , separating the $\nu = 0$ and $\nu = 1$ regimes, and a flat band of MKPs emerge between the projected nodes [63] at the edge along \hat{y} .

Figure 3(a) illustrates a representative phase diagram in the Ω - Δ plane. Indeed, all three phases emerge and the nodal superfluid intervenes the normal and topological ones. Surprisingly, we find that the nodes are Dirac points with linear dispersions and topological protections. Diagonalizing Eq. (8) yields the phase boundaries and the Dirac point positions, as determined by

$$\xi_{k_x}^2 + \Delta^2 = \Omega^2, \quad 4\alpha^2 \sin^2 k_x = t_1^2 + t_2^2 + 2t_1 t_2 \cos k_y. \quad (10)$$

The Dirac points are two-fold degenerate and come in multiples of four, as dictated by the \tilde{T} and \mathcal{M} symmetries that respectively flip k_x and k_y . Moreover, any loop enclosing one such Dirac point has a total winding number $\gamma_t = \pm 1$ [63], protected by an emergent chiral symmetry

$$\tilde{\mathcal{C}} \mathcal{H}_k^{\text{BdG}} \tilde{\mathcal{C}}^{-1} = -\mathcal{H}_k^{\text{BdG}}, \quad \tilde{\mathcal{C}} = \tau_y \sigma_y. \quad (11)$$

Figure 3(b) displays the four Dirac points and their γ_t 's accordingly. Figures 3(c) and 3(d) contrast the MKP edge flat bands in the Dirac-nodal and topological superfluids.

Discussion.—It is instructive to consider the stability of MKPs and their flat bands in our proposed scheme. For an array of topological superfluids without the \tilde{T} and \mathcal{M} symmetries, it is known that Majoranas interactions spontaneously produce nonuniform pairing fields $\Delta_j e^{i\phi_j}$ and edge supercurrent loops [61]. Since the phase fluctuations cannot be gauged away, the Majoranas can be gapped out in pairs. Neglecting long-range interactions, the Majorana annihilation is governed by the nearest-neighbor Josephson couplings as follows [60]:

$$\delta H = - \sum_{\langle ij \rangle} [J_0 \cos \phi_{ij} + i J_{ij} \gamma_i \gamma_j \sin(\phi_{ij}/2)], \quad (12)$$

with $J_0, J_{ij} > 0$ and $\phi_{ij} = \phi_i - \phi_j$. While the first term favors a global phase coherence, the second term splits the Majorana zero modes through phase fluctuations.

In sharp contrast, the MKP flat bands of our system are robust against such phase fluctuations. This can be best understood from the symmetry perspective. Under the \mathcal{M} operation, the local pairing term

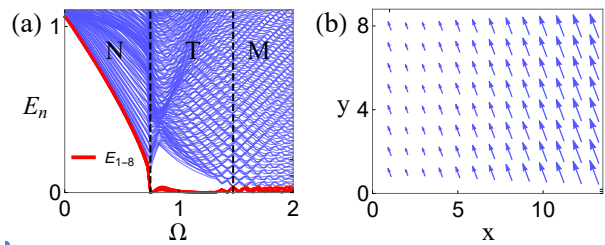


FIG. 4: (a) Self-consistent quasiparticle spectrum for the 100×8 lattice model. The red lines denote the eight lowest quasiparticle excitation states. (b) Vector plot of the local pairing fields $\Delta_j e^{i\phi_j}$ for $\Omega = 1.1$. The length (direction) of each arrow denotes the strength (phase) of the local pairing field. $t_1 = t_2 = 0.5$, $\alpha = 1$, and $\mu = -2$ are used in (a)-(b).

$\Delta_i e^{i\phi_i} c_{i\uparrow} c_{i\downarrow}$ becomes $\Delta_i e^{i\phi_i} c_{i+1\uparrow} c_{i+1\downarrow}$ since the sublattice and spin indices in Eq. (8) are simultaneously flipped. For the Josephson coupling, the J_{ij} -term must vanish as $\phi_i = \phi_{i+1}$ is dictated by mirror symmetry.

Our self-consistent calculations also agree with such a symmetry argument. Fig. 4(a) plots the BdG spectrum for a 100×8 lattice model of Eq. (8). Consistent with Fig. 3(a), the system undergoes two transitions as the Zeeman field increases: from a normal superfluid to a topological one and eventually to a metal phase with $\langle \Delta \rangle = 0$. (Dirac points are absent due to the finite size effect.) The topological phase hosts eight-fold degenerate zero modes on the boundary along \hat{y} , forming a MKP flat band that is also stable against the t_1 - t_2 anisotropy. These remarkable features suggest that our proposed scheme is superior to previous ones.

Finally, a few comments are in order on relevant experiments. In the 2D setup, the Zeeman field switches sign between neighboring chains of distance b . This can be realized through the periodic modulation $\Omega_1 \sim \cos(\pi y/b)$ for one Raman laser. Such a modulation can be produced by a digital micromirror device [70, 73, 74], which can generate an arbitrary modulation of laser intensity. This setup can be generalized to a 3D lattice with $\Omega_1 \sim \cos(\pi y/b) \cos(\pi z/c)$, where a boundary MKP flat band is anticipated. Our scheme of restoring TR symmetry via a spatial reflection can be generalized to various different systems, where the SOCs have been realized for other types of pseudospin states [75–78].

The MKPs can be experimentally detected using spatially resolved radio-frequency spectroscopy [70, 79–83], which measures the local density of states, similar to scanning tunneling microscope. Different from a single Majorana mode, the intrinsic two-fold degeneracy of a MKP can be further affirmed from the energy splitting and spatial separation of two Majoranas due to symmetry breaking [70], which can be induced by the imbalance of Ω between the two chains. Our results not only provide a simple experimental scheme for realizing mirror- and TR-invariant topological and Dirac-nodal superfluids

but also establish a unique platform for exploring MKPs and their applications in quantum computation.

Note added.—Near the submission of this manuscript, we became aware of an independent work [84] that explores MKPs in double semiconductor nanowires with proximity-induced s-wave pairing and *ad hoc* opposite Zeeman fields. While pairing fluctuation, mirror symmetry, Dirac phase, and flat band are not discussed in Ref. [84], the results based on the emergent time-reversal symmetry in the two works agree with each other.

H.H. and C.Z. are supported by NSF (PHY-1505496, PHY-1806227), ARO (W911NF-17-1-0128), AFOSR (FA9550-16-1-0387). F.Z. is supported by UTD (Research Enhancement Funds) and ARO (W911NF-18-1-0416).

* Electronic address: chuanwei.zhang@utdallas.edu

- [1] M. Z. Hasan and C. L. Kane, *Colloquium: Topological insulators*, *Rev. Mod. Phys.* **82**, 3045 (2010).
- [2] X.-L. Qi and S.-C. Zhang, *Topological insulators and superconductors*, *Rev. Mod. Phys.* **83**, 1057 (2011).
- [3] Y.-J. Lin, K. Jiménez-García, and I. B. Spielman, *Spin-orbit-coupled Bose-Einstein condensates*, *Nature* **471**, 83 (2011).
- [4] Z. K. Fu, P. J. Wang, S. J. Chai, L. H. Huang, and J. Zhang, *Bose-Einstein condensate in a light-induced vector gauge potential using 1064-nm optical-dipole-trap lasers*, *Phys. Rev. A* **84**, 043609 (2011).
- [5] J.-Y. Zhang et al., *Collective Dipole Oscillations of a Spin-Orbit Coupled Bose-Einstein Condensate*, *Phys. Rev. Lett.* **109**, 115301 (2012).
- [6] C. Qu, C. Hamner, M. Gong, C. Zhang, and P. Engels, *Observation of Zitterbewegung in a spin-orbit coupled Bose-Einstein condensate*, *Phys. Rev. A* **88**, 021604(R) (2013).
- [7] A. J. Olson, S.-J. Wang, R. J. Niffenegger, C.-H. Li, C. H. Greene, and Y. P. Chen, *Tunable Landau-Zener transitions in a spin-orbit-coupled Bose-Einstein condensate*, *Phys. Rev. A* **90**, 013616 (2014).
- [8] P. Wang, Z.-Q. Yu, Z. Fu, J. Miao, L. Huang, S. Chai, H. Zhai, and J. Zhang, *Spin-Orbit Coupled Degenerate Fermi Gases*, *Phys. Rev. Lett.* **109**, 095301 (2012).
- [9] L. W. Cheuk, A. T. Sommer, Z. Hadzibabic, T. Yefsah, W. S. Bakr, and M. W. Zwierlein, *Spin-Injection Spectroscopy of a Spin-Orbit Coupled Fermi Gas*, *Phys. Rev. Lett.* **109**, 095302 (2012).
- [10] R. A. Williams, M. C. Beeler, L. J. LeBlanc, and I. B. Spielman, *Raman-Induced Interactions in a Single-Component Fermi Gas Near an s-Wave Feshbach Resonance*, *Phys. Rev. Lett.* **111**, 095301 (2013).
- [11] L. Huang, Z. Meng, P. Wang, P. Peng, S.-L. Zhang, L. Chen, D. Li, Q. Zhou, and J. Zhang, *Experimental realization of two-dimensional synthetic spin-orbit coupling in ultracold Fermi gases*, *Nat. Phys.* **12**, 540 (2016).
- [12] Z. Meng, L. Huang, P. Peng, D. Li, L. Chen, Y. Xu, C. Zhang, P. Wang, and J. Zhang, *Experimental Observation of a Topological Band Gap Opening in Ultracold Fermi Gases with Two-Dimensional Spin-Orbit Coupling*, *Phys. Rev. Lett.* **117**, 235304 (2016).
- [13] Z. Wu, L. Zhang, W. Sun, X.-T. Xu, B.-Z. Wang, S.-C. Ji, Y. Deng, S. Chen, X.-J. Liu, J.-W. Pan, *Realization of two-dimensional spin-orbit coupling for Bose-Einstein condensates*, *Science* **354**, 83 (2016).
- [14] C. Zhang, S. Tewari, R. M. Lutchyn, and S. Das Sarma, *$p_x + ip_y$ Superfluid from s-Wave Interactions of Fermionic Cold Atoms*, *Phys. Rev. Lett.* **101**, 160401 (2008).
- [15] M. Sato, Y. Takahashi, and S. Fujimoto, *Non-Abelian Topological Order in s-Wave Superfluids of Ultracold Fermionic Atoms*, *Phys. Rev. Lett.* **103**, 020401 (2009).
- [16] L. Jiang et al., *Majorana fermions in equilibrium and in driven cold-atom quantum chains*, *Phys. Rev. Lett.* **106**, 220402 (2011).
- [17] F. Wilczek, *Majorana returns*, *Nat. Phys.* **5**, 614 (2009).
- [18] J. Alicea, *New directions in the pursuit of Majorana fermions in solid state systems*, *Rep. Prog. Phys.* **75**, 076501 (2012).
- [19] M. Franz, *Majorana's chains*, *Nat. Nano.* **8**, 149 (2013).
- [20] A. Y. Kitaev, *Fault-tolerant quantum computation by anyons*, *Ann. Phys.* **303**, 2 (2003).
- [21] L. Fu and C. L. Kane, *Superconducting proximity effect and Majorana fermions at the surface of a topological insulator*, *Phys. Rev. Lett.* **100**, 096407 (2008).
- [22] R. M. Lutchyn, J. D. Sau, and S. Das Sarma, *Majorana fermions and a topological phase transition in semiconductor-superconductor heterostructures*, *Phys. Rev. Lett.* **105**, 077001 (2010).
- [23] Y. Oreg, G. Refael, and F. von Oppen, *Helical liquids and Majorana bound states in quantum chains*, *Phys. Rev. Lett.* **105**, 177002 (2010).
- [24] J. D. Sau, R. M. Lutchyn, S. Tewari, and S. Das Sarma, *Generic new platform for topological quantum computation using semiconductor heterostructures*, *Phys. Rev. Lett.* **104**, 040502 (2010).
- [25] S. Tewari, S. Das Sarma, C. Nayak, C. Zhang, and P. Zoller, *Quantum computation using vortices and Majorana zero modes of a $p_x + ip_y$ superfluid of fermionic cold atoms*, *Phys. Rev. Lett.* **98**, 010506 (2007).
- [26] J. Alicea, *Majorana fermions in a tunable semiconductor device*, *Phys. Rev. B* **81**, 125318 (2010).
- [27] T. D. Stanescu, R. M. Lutchyn, and S. Das Sarma, *Majorana fermions in semiconductor nanochains*, *Phys. Rev. B* **84**, 144522 (2011).
- [28] J. Alicea, Y. Oreg, G. Refael, F. von Oppen, and M. P. A. Fisher, *Non-Abelian statistics and topological quantum information processing in 1D chain networks*, *Nat. Phys.* **7**, 412 (2011).
- [29] X.-L. Qi, T. L. Hughes, and S.-C. Zhang, *Chiral topological superconductor from the quantum Hall state*, *Phys. Rev. B* **82**, 184516 (2010).
- [30] A. C. Potter and P. A. Lee, *Multichannel generalization of Kitaev's Majorana end states and a practical route to realize them in thin films*, *Phys. Rev. Lett.* **105**, 227003 (2010).
- [31] V. Mourik et al., *Signatures of Majorana fermions in hybrid superconductor-semiconductor nanochain devices*, *Science* **336**, 1003 (2012).
- [32] S. Nadj-Perge et al., *Observation of Majorana fermions in ferromagnetic atomic chains on a superconductor*, *Science* **346**, 602 (2014).
- [33] A. Das et al., *Zero-bias peaks and splitting in an Al-InAs nanochain topological superconductor as a signature of*

- Majorana fermions*, *Nat. Phys.* **8**, 887 (2012).
- [34] H. O. H. Churchill et al., *Superconductor-nanochain devices from tunneling to the multichannel regime: zero-bias oscillations and magnetoconductance crossover*, *Phys. Rev. B* **87**, 241401(R) (2013).
- [35] M.-X. Wang et al., *The coexistence of superconductivity and topological order in the Bi_2Se_3 thin films*, *Science* **336**, 52 (2012).
- [36] A. D. K. Finck, D. J. Van Harlingen, P. K. Mohseni, K. Jung, and X. Li, *Anomalous modulation of a zero-bias peak in a hybrid nanochain-superconductor device*, *Phys. Rev. Lett.* **110**, 126406 (2013).
- [37] S. Tewari and J. D. Sau, *Topological Invariants for Spin-Orbit Coupled Superconductor Nanowires*, *Phys. Rev. Lett.* **109**, 150408 (2012).
- [38] A. P. Schnyder, S. Ryu, A. Furusaki, and A. W. W. Ludwig, *Classification of Topological Insulators and Superconductors*, *AIP Conf. Proc.* **1134**, 10 (2009).
- [39] A. Kitaev, *Periodic table for topological insulators and superconductors*, *AIP Conf. Proc.* **1134**, 22 (2009).
- [40] X.-L. Qi, T. L. Hughes, S. Raghu, and S.-C. Zhang, *Time-reversal-invariant topological superconductors and superfluids in two and three dimensions*, *Phys. Rev. Lett.* **102**, 187001 (2009).
- [41] F. Zhang, C. L. Kane, and E. J. Mele, *Time-reversal-invariant topological superconductivity and Majorana Kramers pairs*, *Phys. Rev. Lett.* **111**, 056402 (2013).
- [42] F. Zhang, C. L. Kane, and E. J. Mele, *Topological mirror superconductivity*, *Phys. Rev. Lett.* **111**, 056403 (2013).
- [43] C. L. M. Wong and K. T. Law, *Majorana Kramers doublets in $d_{x^2-y^2}$ -wave superconductors with Rashba spin-orbit coupling*, *Phys. Rev. B* **86**, 184516 (2012).
- [44] F. Zhang and C. L. Kane, *Anomalous topological pumps and fractional Josephson effects*, *Phys. Rev. B* **90**, 020501(R) (2014).
- [45] X.-J. Liu, C. L. M. Wong, and K. T. Law, *Non-Abelian Majorana doublets in time-reversal-invariant topological superconductors*, *Phys. Rev. X* **4**, 021018 (2014).
- [46] F. Zhang and C. L. Kane, *Time-reversal-invariant Z_4 fractional Josephson effect*, *Phys. Rev. Lett.* **113**, 036401 (2014).
- [47] Z.-q. Bao and F. Zhang, *Topological Majorana Two-Channel Kondo Effect*, *Phys. Rev. Lett.* **119**, 187701 (2017).
- [48] C.-X. Liu, Björn Trauzettel, *Helical Dirac-Majorana interferometer in a superconductor/topological insulator sandwich structure*, *Phys. Rev. B* **83**, 220510(R) (2011).
- [49] S. Nakosai, Y. Tanaka, and N. Nagaosa, *Topological superconductivity in bilayer Rashba system*, *Phys. Rev. Lett.* **108**, 147003 (2012).
- [50] S. Deng, L. Viola, and G. Ortiz, *Majorana modes in time-reversal invariant s-wave topological superconductors*, *Phys. Rev. Lett.* **108**, 036803 (2012).
- [51] S. Nakosai, J. C. Budich, Y. Tanaka, B. Trauzettel, and N. Nagaosa, *Majorana bound states and nonlocal spin correlations in a quantum chain on an unconventional superconductor*, *Phys. Rev. Lett.* **110**, 117002 (2013).
- [52] A. Keselman, L. Fu, A. Stern, and E. Berg, *Inducing time-reversal-invariant topological superconductivity and fermion parity pumping in quantum chains*, *Phys. Rev. Lett.* **111**, 116402 (2013).
- [53] E. Gaidamauskas, J. Paaske, and K. Flensberg, *Majorana bound states in two-channel time-reversal-symmetric nanochain systems*, *Phys. Rev. Lett.* **112**, 126402 (2014).
- [54] J. Wang, Y. Xu, and S.-C. Zhang, *Two-dimensional time-reversal-invariant topological superconductivity in a doped quantum spin-Hall insulator*, *Phys. Rev. B* **90**, 054503 (2014).
- [55] J. Klinovaja, A. Yacoby, and D. Loss, *Kramers pairs of Majorana fermions and parafermions in fractional topological insulators*, *Phys. Rev. B* **90**, 155447 (2014).
- [56] C. Schrade, A. A. Zyuzin, J. Klinovaja, and D. Loss, *Proximity-induced π Josephson junctions in topological insulators and Kramers pairs of Majorana fermions*, *Phys. Rev. Lett.* **115**, 237001 (2015).
- [57] Y. Y. Huang, C.-K. Chiu, *Helical Majorana edge mode in a superconducting antiferromagnetic quantum spin Hall insulator*, arXiv:1708.05724.
- [58] Q. Wang, C.-C. Liu, Y.-M. Lu, and Fan Zhang, *High-temperature Majorana corner states*, *Phys. Rev. Lett.* **121**, 186801 (2018).
- [59] Click to see the proposed no-go theorem.
- [60] Y. Li, D. Wang, and C. Wu, *Spontaneous breaking of time-reversal symmetry in the orbital channel for the boundary Majorana flat bands*, *New J. Phys.* **15**, 085002 (2013).
- [61] D. Wang, Z. S. Huang, C. Wu, *The fate and remnant of Majorana zero modes in a quantum chain array*, *Phys. Rev. B* **89**, 174510 (2014).
- [62] T. P. Meyrath, F. Schreck, J. L. Hanssen, C.-S. Chuu, M.G. Raizen, *A high frequency optical trap for atoms using Hermite-Gaussian beams*, *Opt. Express* **13**, 2843 (2005).
- [63] S. A. Yang, H. Pan, and F. Zhang, *Dirac and Weyl superconductors in three dimensions*, *Phys. Rev. Lett.* **113**, 046401 (2014).
- [64] J. Brand, L. A. Toikka, and U. Zuehlcke, *Accurate projective two-band description of topological superfluidity in spin-orbit-coupled Fermi gases*, *SciPost Phys.* **5**, 016 (2018).
- [65] C. Qu et al., *Topological superfluids with finite-momentum pairing and Majorana fermions*, *Nat. Commun.* **4**, 2710 (2013).
- [66] Y. Xu, C. Qu, M. Gong, and C. Zhang, *Competing superfluid orders in spin-orbit-coupled fermionic cold-atom lattices*, *Phys. Rev. A* **89**, 013607 (2014).
- [67] C. Qu, M. Gong, and C. Zhang, *Fulde-Ferrell-Larkin-Ovchinnikov or Majorana superfluids: The fate of fermionic cold atoms in spin-orbit-coupled optical lattices*, *Phys. Rev. A* **89**, 053618 (2014).
- [68] Y. Xu, L. Mao, B. Wu, and C. Zhang, *Dark solitons with Majorana fermions in spin-orbit-coupled Fermi gases*, *Phys. Rev. Lett.* **113**, 130404 (2014).
- [69] L. Jiang et al., *Spin-orbit-coupled topological Fulde-Ferrell states of fermions in a harmonic trap*, *Phys. Rev. A* **90**, 053606 (2014).
- [70] See “Supplementary Materials” for more discussions on the topological invariants, validity of the double-chain model, continuum models, and experimental detections.
- [71] J. C. Budich and E. Ardonne, *Topological invariant for generic one-dimensional time-reversal-symmetric superconductors in class DIII*, *Phys. Rev. B* **88**, 134523 (2013).
- [72] L. Chen, T. Mazaheri, A. Seidel, and X. Tang, *The impossibility of exactly flat non-trivial Chern bands in strictly local periodic tight binding models*, *J. Phys. A: Math. Theor.* **47**, 152001 (2014).
- [73] P. Zupancic et al., *Ultra-precise holographic beam shaping for microscopic quantum control*, *Opt. Express* **24**, 13881

- (2016).
- [74] M. E. Tai *et al.*, *Microscopy of the interacting Harper–Hofstadter model in the two-body limit*, *Nature* **546**, 519 (2017).
 - [75] J.-R. Li *et al.*, *A stripe phase with supersolid properties in spin-orbit-coupled Bose-Einstein condensates*, *Nature* **543**, 91 (2017).
 - [76] J. Li *et al.*, *Spin-orbit coupling and spin textures in optical superlattices*, *Phys. Rev. Lett.* **117**, 185301 (2016).
 - [77] S. Kolkowitz *et al.*, *Spin-orbit-coupled fermions in an optical lattice clock*, *Nature* **542**, 66 (2017).
 - [78] M. L. Wall *et al.*, *Synthetic spin-orbit coupling in an optical lattice clock*, *Phys. Rev. Lett.* **116**, 035301 (2016).
 - [79] C. A. Regal and D. S. Jin, *Measurement of positive and negative scattering lengths in a Fermi gas of atoms*, *Phys. Rev. Lett.* **90**, 230404 (2003).
 - [80] S. Gupta *et al.*, *Radio-frequency spectroscopy of ultracold fermions*, *Science* **300**, 1723 (2003).
 - [81] C. Chin *et al.*, *Observation of the pairing gap in a strongly interacting Fermi gas*, *Science* **305**, 1128 (2004).
 - [82] Y. Shin, C. H. Schunck, A. Schirotzek, and W. Ketterle, *Tomographic rf spectroscopy of a trapped Fermi gas at unitarity*, *Phys. Rev. Lett.* **99**, 090403 (2007).
 - [83] L. Jiang, L. O. Baksmaty, H. Hu, Y. Chen, and H. Pu, *Single impurity in ultracold Fermi superfluids*, *Phys. Rev. A* **83**, 061604(R) (2011).
 - [84] C. Reeg, C. Schrade, J. Klinovaja, and D. Loss, *DIII topological superconductivity with emergent time-reversal symmetry*, *Phys. Rev. B* **96**, 161407(R) (2017).

Supplementary Materials

Topological Invariant and Mirror Symmetry

In the main text, we have derived the \mathbb{Z}_2 topological invariant ν directly using the mirror symmetry \mathcal{M} . Here, we give more details on the construction of this \mathbb{Z}_2 invariant, which classifies time-reversal (TR) invariant topological superfluids in 1D and 2D.

I. 1D Case

The mirror symmetry \mathcal{M} is a spatial symmetry with $\mathcal{M}^2 = -1$. As $[\mathcal{M}, \mathcal{H}_k^{BdG}] = 0$, the Hamiltonian can be decomposed into two sectors, with each sector belonging to a specific subspace labeled by one of the two mirror eigenvalues $\pm i$. Mathematically, the 8×8 Hamiltonian Eq. (1) in the main text can be block-diagonalized as $U_1 \mathcal{H}_k^{BdG} U_1^\dagger = h(k) \oplus h^*(-k)$ by the transformation U_1 such that $U_1 \mathcal{M} U_1^\dagger = i \text{diag}(I_{4 \times 4}, -I_{4 \times 4})$ and $h(k)$ reads

$$h(k) = \begin{pmatrix} -\xi_k + \Omega & -i\alpha_k & \Delta & 0 \\ i\alpha_k & -\xi_k - \Omega & 0 & \Delta \\ \Delta & 0 & \xi_k + \Omega & i\alpha_k \\ 0 & \Delta & -i\alpha_k & \xi_k - \Omega \end{pmatrix}, \quad (13)$$

with $\xi_k = -2t \cos k - \mu$, $\alpha_k = 2\alpha \sin k - t_\perp$. As the eigenvalues $\pm i$ switch signs under the individual action of anti-unitary TR or particle-hole operator, each eigen-block has neither TR nor particle-hole symmetries, whereas it remains invariant under the co-action of these two symmetries, i.e., the chiral symmetry \mathcal{C} . Thus, each mirror eigen-block belongs to the AIII symmetry class in the Altland-Zirnbauer table [42], labeled by opposite 1D winding numbers [42]. The latter is because the two eigen-blocks are related by the TR symmetry. To see this fact, consider $|\phi\rangle$ as an eigenstate of \mathcal{M} with mirror eigenvalue i . Since $\mathcal{M}(\tilde{\mathcal{T}}|\phi\rangle) = \tilde{\mathcal{T}}\mathcal{M}|\phi\rangle = \tilde{\mathcal{T}}(i|\phi\rangle) = -i\tilde{\mathcal{T}}|\phi\rangle$, $\tilde{\mathcal{T}}|\phi\rangle$ is also an eigenstate of \mathcal{M} but with mirror eigenvalue $-i$.

Now we focus on the $h(k)$ sector. The chiral symmetry operator can be chosen as $\mathcal{C}_{\mathcal{M}=i} = \tau_y \otimes \sigma_y$ with $\{\mathcal{C}_{\mathcal{M}=i}, h(k)\} = 0$. To construct the topological invariant, we can choose a unitary transformation U_2 such that $U_2 \mathcal{C}_{\mathcal{M}=i} U_2^\dagger = \text{diag}(I_{2 \times 2}, -I_{2 \times 2})$. In this new basis, $h(k)$ can be rewritten in the off-diagonal form as follows:

$$U_2 h(k) U_2^\dagger = \begin{pmatrix} 0 & g(k) \\ g^\dagger(k) & 0 \end{pmatrix}, \quad g(k) = \begin{pmatrix} \xi_k - \Omega & -\Delta - i\alpha_k \\ \Delta + i\alpha_k & \xi_k + \Omega \end{pmatrix}. \quad (14)$$

With the evolution of k from 0 to 2π , the trajectory of the complex function $z(k) \equiv \det g(k)$ forms a closed curve on the cylinder, characterized by the following winding number

$$\gamma_+ = \frac{1}{2\pi i} \oint_0^{2\pi} \frac{dz(k)}{z(k)}. \quad (15)$$

If we take into account both mirror subspaces, the \mathbb{Z}_2 topological invariant can be formulated as $\nu = \gamma_+ \bmod 2$, consistent with a previous theory [42]. Note that the TR symmetry requires the winding numbers to be opposite for the two mirror subspaces: $\gamma_+ = -\gamma_-$; by defining $\gamma_m = (\gamma_+ - \gamma_-)/2$ we obtain $\nu = \gamma_m \bmod 2$.

An intuitive view of the trajectories of $z(k)$ in different phases is illustrated in Fig. 5. The system is a normal superfluid when $|\Omega| < \Omega_{c_1}$. The evolution of k from 0 to 2π results in a contractible path on the cylinder surface [Fig. 5(a)], indicating $\nu = \gamma_m = 0$. For the TR invariant topological (mirror) superfluid with $\Omega_{c_1} < |\Omega| < \Omega_{c_2}$, the path is non-contractible around the cylinder [Fig. 5(b)], indicating $\nu = \gamma_m = 1$. Further increasing Zeeman field to $|\Omega| > \Omega_{c_2}$, the system reenters into the normal superfluid phase with a contractible path [Fig. 5(c)]. The validity of the \mathbb{Z}_2 invariant ν has been further confirmed by the quasiparticle spectrum under the open boundary condition. For topological superfluid, there exists a pair of degenerate zero modes, i.e., Majorana Kramers pair (MKP), localized on each end due to the TR symmetry. For normal superfluid, no zero modes emerge in the bulk gap.

II. 2D Case

For the 2D Hamiltonian Eq. (8) in the main text, the TR symmetry is $\tilde{\mathcal{T}} \mathcal{H}^{BdG}(k_x, k_y) \tilde{\mathcal{T}}^{-1} = \mathcal{H}^{BdG}(-k_x, k_y)$, which relates (k_x, k_y) and $(-k_x, k_y)$. For each k_y , the effective 1D system belongs to the symmetry class DIII, which

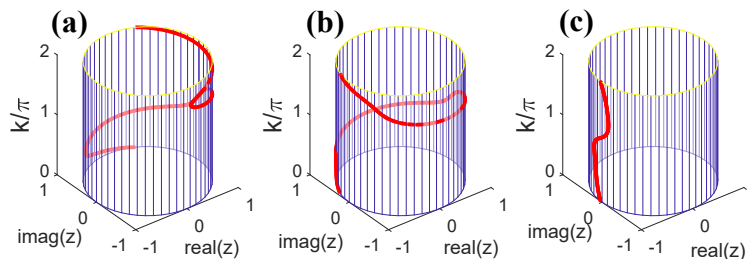


FIG. 5: Winding of $z(k)/|z(k)|$ in different phases. (a) Normal superfluid, $\Omega = 0.5$. (b) TR invariant topological superfluid, $\Omega = 2$. (c) Normal superfluid, $\Omega = 5$. We have used $\mu = -2$, $\Delta = 1$, $t = 1$, $\alpha = 1$, and $t_{\perp} = 0.5$; the phase boundaries [see Eq. (6) in the main text] are $\Omega_{c_1} \approx 1.002$ and $\Omega_{c_2} \approx 4.0615$.

is characterized by a \mathbb{Z}_2 invariant ν_{k_y} . As a consequence, there exist three topologically distinct superfluid phases:

$$\begin{cases} \text{Normal superfluid,} & \nu_{k_y} = 0 \text{ for all } k_y; \\ \text{TR-invariant topological superfluid,} & \nu_{k_y} = 1 \text{ for all } k_y; \\ \text{Dirac-nodal superfluid,} & \nu_{k_y} = 0 \text{ or } 1. \end{cases} \quad (16)$$

For a TR invariant topological superfluid, there emerge MKP edge flat bands from $k_y = -\pi$ to π in the open boundary condition. The Dirac-nodal superfluid is gapless, whereas the 1D Brillouin zones at fixed k_y values are divided into several topologically distinct regions, labeled by either $\nu_{k_y} = 0$ or $\nu_{k_y} = 1$. The bulk gap must close at the Dirac points, and these Dirac points can be regarded as topological phase transition points for the effective 1D models. Thus, in the open boundary condition, there are MKP edge flat bands connecting the projected Dirac points. Totally, there are four Dirac points as dictated by both the TR and mirror symmetries.

Validity of the double-chain Model

Our primary model Eq. (1) in the main text describes two coupled 1D Fermi gases experiencing the same spin-orbit coupling (SOC) but opposite Zeeman fields introduced by the Hermite-Gaussian beam. To generate the double-chain structure, a double well trapping potential along the y direction is needed. The tunneling t_{\perp} between the two Fermi gases (i.e., the kinetic energy along the y direction) depends on the depth of the double well trapping potential in the y direction, which is tunable. In the following, we show the validity of the tight-binding model Eq. (1) in the main text and provide the details of our calculations and estimations. Since the realized SOC $\alpha k_x \sigma_y$ is intrinsically 1D, the movements along the x and y directions are independent. The dynamics along the y direction is governed by the following single-particle Hamiltonian:

$$H_y = -\frac{\hbar^2 \partial_y^2}{2m} + \Omega(y) \sigma_z + V_{\text{trap}}(y). \quad (17)$$

Here $\Omega(y) = \Omega_0 y e^{-\frac{y^2}{w^2}}$ is the effective Zeeman field induced by the Hermite-Gaussian beam. The trapping potential along the y direction can be approximately described by $V_{\text{trap}}(y) = \frac{1}{2} m \omega_y^2 y^2 + V_0 \cos^2(k_0 y)$, although in practice a double well optical lattice can be used. We numerically solve the eigenstates of H_y , with the lowest two-fold degenerate eigenstates shown in Fig. 6.

Obviously, the ground state mainly resides on the potential minimum for each spin species, validating our tight-binding approximation in the y direction. A rough approximation of t_{\perp} can be obtained from the 1D Mathieu equation $t_{\perp} \approx \frac{4}{\sqrt{\pi}} \left(\frac{V_0}{E_r}\right)^{3/4} e^{-2\left(\frac{V_0}{E_r}\right)^{1/2}} = 0.224 E_r$. The Zeeman field $\Omega(y)$ can be controlled by tuning the Hermite-Gaussian beam. Note that in our simulation the condition of large $\Omega(y)$ is not needed for the tight-binding approximation, although a large Zeeman field indeed tends to localize the two ground states at the potential minima.

Continuum model

For the dynamics along the x direction (with 1D SOC), we have considered a lattice model as described by Eq. (1) in the main text. This lattice regularization does not change the essential results. In this section, we consider the

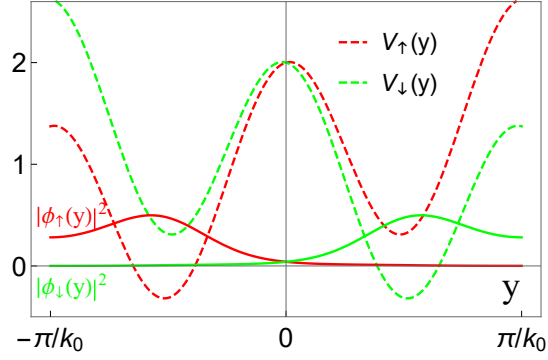


FIG. 6: Effective potentials $V_\sigma(y) = \Omega(y)\sigma_z + V_{\text{trap}}(y)$ in units of E_R and ground state probabilities for spin-up and spin-down atoms. Typical experimental parameters of ^{40}K atoms are used. $k_0 = 2\pi/\lambda$ with $\lambda = 680$ nm, $E_R = 2\pi\hbar \times 10.8$ kHz. For the harmonic trap, $\hbar\omega_y = 0.02E_R$; for the dipole trap, $V_0 = 2E_R$. $\Omega_0 = 0.2k_0E_R$. The waist of the Hermite-Gaussian beam is $2\pi w = 100\lambda$.

continuum version of the 1D BdG Hamiltonian and demonstrate the phase diagram and the emergence of MKPs in the TR invariant topological (mirror) superfluid. As we shall see, the essential physics of the continuum model is the same as that in the lattice model (as shown in the main text).

I. Phase diagram

In the same Nambu basis, the spin-orbit coupled double Fermi gases can be described by the following continuum model Hamiltonian

$$\mathcal{H}_{\text{continuum}}^{\text{BdG}}(k) = \left[\frac{\hbar^2 k^2}{2m} - \tilde{\mu} + 2\alpha k\sigma_y - t_\perp s_x \right] \tau_z + \Omega\sigma_z s_z + \tilde{\Delta}\tau_x. \quad (18)$$

Here k is the particle momentum along x direction, $\tilde{\mu}$ is the chemical potential, and $\alpha = \hbar^2 k_r/2m$ is the SOC strength, with k_r the recoil momentum [8, 9]. The lattice model Eq. (1) in the main text can be obtained from the above continuum model via the standard substitution: $\sin k \leftrightarrow k$, $\cos k \leftrightarrow 1 - k^2/2$. The pairing order parameter is defined as $\tilde{\Delta} = g \sum_k \langle c_{-k\downarrow} c_{k\uparrow} \rangle$, with g (< 0) the attractive inter-particle interaction. The transverse tunneling t_\perp can be tuned by adjusting the trap depth in the y direction. For simplicity, we take the recoil energy $E_r = \hbar^2 k_r^2/2m$ and the recoil momentum k_r as natural energy and momentum units (or equivalently by setting $\hbar = 2m = 1$ in Eq. (18)).

For the above continuum model Hamiltonian, the transition between the topological and normal superfluids (i.e., the condition for gap closure) is determined by the critical Zeeman field strength

$$\Omega_c = \sqrt{\left(\frac{t_\perp^2}{4} - \tilde{\mu}\right)^2 + \tilde{\Delta}^2}. \quad (19)$$

For $\Omega < \Omega_c$ the superfluid is normal, whereas for $\Omega > \Omega_c$, the superfluid is topological and hosts MKPs on its boundary. Now we self-consistently calculate the phase diagram of the continuum model. At zero temperature, the thermodynamical potential $\Omega_{\text{TP}} = -(1/\beta) \log \text{Tr} e^{-\beta[\sum_k H_{\text{continuum}}^{\text{BdG}}(k) - \tilde{\mu}N]}$ (with $\beta = 1/k_B T$) reduces to

$$\Omega_{\text{TP}} = \sum_k (k^2 - \tilde{\mu}) + \sum_{E_{n,k} < 0} E_{n,k} - \frac{|\tilde{\Delta}|^2}{g}. \quad (20)$$

Here $E_{n,k}$ is the n -th eigenenergy of $H_{\text{continuum}}^{\text{BdG}}(k)$. The phase diagram can be analytically obtained by minimizing Ω_{TP} with respect to the order parameter $\tilde{\Delta}$, i.e., $\partial\Omega_{\text{TP}}/\partial\tilde{\Delta} = 0$. However, due to its complexity, we extract the phase diagram numerically. Note that we should take $\tilde{\mu} = \mu + 2$ to compare with the phase diagram of the lattice model in the main text. (For $k = 0$, the kinetic energy is -2 in the lattice model yet 0 in the continuum model.)

The phase diagram in $\Omega - \tilde{\mu}$ plane is illustrated in Fig. 7(a), which is quite similar to that of the lattice model [see Fig. 2(a) in the main text], especially in the low-energy regime (i.e., small $\tilde{\mu}$). Besides the vacuum phase (V) and metal phase (M) with vanishing pairing, there are two types of superfluid phases with finite pairing order parameters $\tilde{\Delta}$.

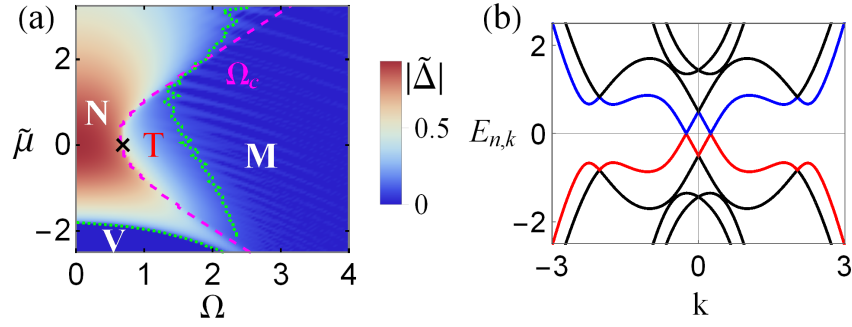


FIG. 7: (a) Phase diagram of the continuum model. The dashed magenta line denotes the critical Zeeman field Ω_c determined by Eq. (19). The dotted cyan lines mark the phase boundaries with reference pairing $|\tilde{\Delta}| = 0.05$. Totally there are four different phases: vacuum phase (V), normal superfluid (N), topological superfluid (T) and metal phase (M). (b) Band crossings at the phase transition point shown by “x” in (a); $\tilde{\mu} = 0$, $\Omega \approx 0.68$, and $t_{\perp} = 0.5$.

The topological superfluid (T) resides between the normal superfluid (N) and metal phase, with the critical Zeeman field strength Ω_c determined by Eq. (19). Note that, due to the lack of lattice, there is no band insulator phase. The quasiparticle spectrum at the phase transition point between the normal and topological superfluids is shown in Fig. 7(b), where the central two bands cross at $k = \pm t_{\perp}/2$.

II. Emergence of MKPs on the boundary

The topological properties of the above TR-invariant topological superfluid phase are characterized by the appearance of MKPs on the boundary. This can be easily demonstrated by self-consistently solving the following real-space BdG equation:

$$H_{\text{BdG}}(x)\Psi_n(x) = E_n\Psi_n(x), \quad (21)$$

where $\Psi_n(x) \equiv [u_n^{1\uparrow}(x), u_n^{1\downarrow}(x), u_n^{2\uparrow}(x), u_n^{2\downarrow}(x), v_n^{1\uparrow}(x), v_n^{1\downarrow}(x), v_n^{2\uparrow}(x), v_n^{2\downarrow}(x)]^T$ is the eight-component wave function of the real-space Hamiltonian $H_{\text{BdG}}(x)$ obtained by the substitution $k \rightarrow -i\partial_x$ in the momentum-space Hamiltonian Eq. (18). The local pairing of each Fermi gas ($s = 1, 2$) is represented by $\tilde{\Delta}^s(x) = g \sum_n [u_n^{s\downarrow} v_n^{s\uparrow*} f(-E_n) + u_n^{s\uparrow} v_n^{s\downarrow*} f(E_n)]$. Here $f(x) = 1/(e^{x/k_B T} + 1)$ the Fermi distribution function, and at zero temperature it reduces to the Heaviside step function.

To examine the existence of MKPs in the topological superfluid, we employ an open boundary condition at $x = 0$ and $x = L$. The wave function can be expanded by a set of base functions as follows:

$$\begin{aligned} u_n^{s\uparrow} &= \sum_m A_{nm}^{s\uparrow} \sqrt{\frac{2}{L}} \sin\left(\frac{m\pi x}{L}\right), & u_n^{s\downarrow} &= \sum_m A_{nm}^{s\downarrow} \sqrt{\frac{2}{L}} \sin\left(\frac{m\pi x}{L}\right), \\ v_n^{s\uparrow} &= \sum_m B_{nm}^{s\uparrow} \sqrt{\frac{2}{L}} \sin\left(\frac{m\pi x}{L}\right), & v_n^{s\downarrow} &= \sum_m B_{nm}^{s\downarrow} \sqrt{\frac{2}{L}} \sin\left(\frac{m\pi x}{L}\right). \end{aligned} \quad (22)$$

To obtain the eigenspectrum of Eq. (21), we diagonalize the Hamiltonian (of size $8N_c \times 8N_c$) in the chosen basis. In our calculations, the truncation number of the basis is $N_c = 100$.

The quasiparticle spectrum in the open boundary condition is plotted in Fig. 8(a). There exist four-fold degenerate zero modes in the bulk pairing gap due to the TR and particle-hole symmetries and the existence of two ends. Take the $n = 4N_c + 1$ state as an example, the wave function is mainly localized at the two ends ($x = 0$ and L), as seen in Fig. 8(b). By contrast, for a normal superfluid, the quasiparticle spectrum is fully gapped without any in-gap zero mode. All these results clearly show that the essential physics is much the same for the lattice model considered in the main text and the continuum model discussed here.

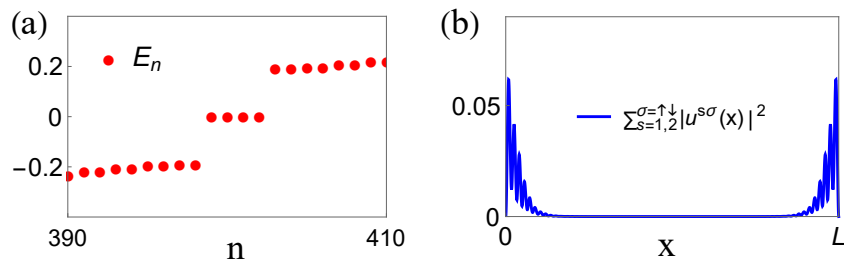


FIG. 8: (a) Quasiparticle spectrum in the open boundary condition, with four-fold degenerate zero modes. (b) Spatial distribution of wave function $\Psi_n(x)$ with $n = 4N_c + 1$. Here $t_\perp = 0.5$, $\tilde{\mu} = 0$, $\Omega = 1$, and $N_c = 100$.

Digital micromirror device and application

In this section, we explain how to obtain the desired laser fields using the digital micromirror device (DMD). The basic principle is sketched in Fig. 9.

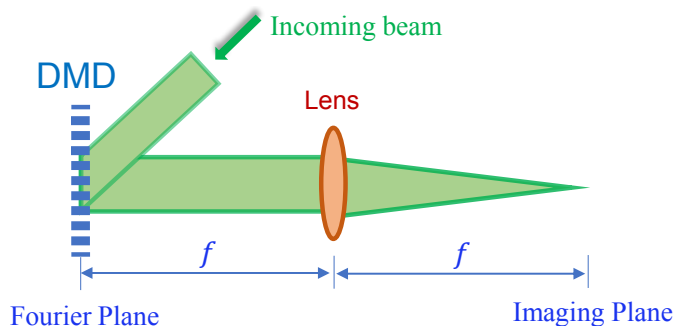


FIG. 9: Schematics of holographic shaping of laser beams.

DMD is an optomechanical spatial light modulator, consisting of many square mirrors. Each mirror can be individually switched between two tilt states (+12 “on” and -12 “off” orientations) and acts as a basic diffractive element under coherent illumination due to its small size. The 2D mirror array forms a reflective grating. The DMDs are employed holographically in the Fourier plane of an imaging system, which enables both local amplitude and phase control simultaneously despite that the direct DMD modulations is binary in intensity. The incoming light is not only reflected into one of the two directions, but it also has a number of diffraction orders. For the m -th diffraction order (in the y direction), the outgoing light field of a single slit of width a centered at y_0 is

$$E_{\text{out}} = E_{\text{in}} \frac{\sin(\pi m a)}{\pi m} e^{i2\pi m y_0}. \quad (23)$$

It is clear that by shifting the slits relative to some reference point, the phase of the diffracted wave fronts can be tuned, while the intensities of the outgoing beams are determined by the width of the slits. Applying these phase and amplitude modifications locally, arbitrary wave fronts can be generated in this way. The downside of the above DMD setup is its relatively low efficiency in laser power. This can be optimized by fulfilling the so-called blazing condition and increasing the intensity of incoming beams. Currently, the DMD-generated laser beams have been widely used to address individual atoms in optical lattices and to manipulate their dynamics.

Experimental detection of MKPs

In this section, we discuss how to detect the MKPs in the topological superfluid phase using the spatially resolved radio-frequency spectroscopy [79–83]. The radio-frequency (rf) field is a probe field to induce single-particle excitation from the fermionic state to an unoccupied fluorescent probe state. The rf signal is directly related to the local density of states (LDOS), similar to that of scanning tunneling microscope. The LDOS for the chain- s contains both spin

components $\rho_s(j, \omega) = \rho_{s\uparrow}(j, \omega) + \rho_{s\downarrow}(j, \omega)$. In the BdG representation,

$$\rho_{s\sigma}(j, \omega) = \frac{1}{2} \sum_{\eta} |u_{\eta}^{s\sigma}(j)|^2 \delta(\omega - E_{\eta}) + |v_{\eta}^{s\sigma}(j)|^2 \delta(\omega + E_{\eta}). \quad (24)$$

We numerically calculate the LDOS for the double-chain lattice system (Eq. (1) in the main text) under a weak harmonic trapping potential $V(j) = w_x^2(j - \frac{L+1}{2})^2$. For $w_x \ll 1$, i.e., the characteristic length of the harmonic trap is much larger than other length scales, local density approximation (LDA) $\mu(j) = \mu - V(j)$ can be used to analyze the local excitations in real space.

The main results are shown in Fig. 10. The harmonic trap separates the system into topologically distinct regions: TR-invariant topological superfluid around the trap center and normal superfluids at the two wings. The boundary between two spatially separated phases is approximately determined by substituting $\mu \rightarrow \mu(j)$ in Eq. (6) in the main text. According to bulk-boundary correspondence, a MKP emerges at each topological boundary. Note that due to the finite length of the system, the MKPs at the two boundaries slightly hybridize and form quasiparticle levels (two-fold degenerate) and quasihole levels (two-fold degenerate). We denote the wave functions of the degenerate quasiparticle levels as $\phi_a = (u_a^{1\uparrow}, u_a^{1\downarrow}, u_a^{2\uparrow}, u_a^{2\downarrow}, v_a^{1\uparrow}, v_a^{1\downarrow}, v_a^{2\uparrow}, v_a^{2\downarrow})$ ($a = \text{I, II}$). Fig. 10(a) plots their spatial distributions, which are localized on the boundaries between the topological superfluid and normal superfluids. Furthermore, as verified by our numerics, the two-fold degenerate quasiparticle states are related by the TR symmetry as: $\phi_{\text{II}} = \tilde{T}\phi_{\text{I}}$ and $\phi_{\text{I}} = -\tilde{T}\phi_{\text{II}}$. In the form of their components, $u_{\text{I}}^{1\uparrow} = u_{\text{II}}^{2\downarrow}$, $u_{\text{I}}^{1\downarrow} = -u_{\text{II}}^{2\uparrow}$, $u_{\text{I}}^{2\uparrow} = u_{\text{II}}^{1\downarrow}$, and $u_{\text{I}}^{2\downarrow} = -u_{\text{II}}^{1\uparrow}$. Note that the wave functions can always be chosen as real since the real-space BdG Hamiltonian is real.

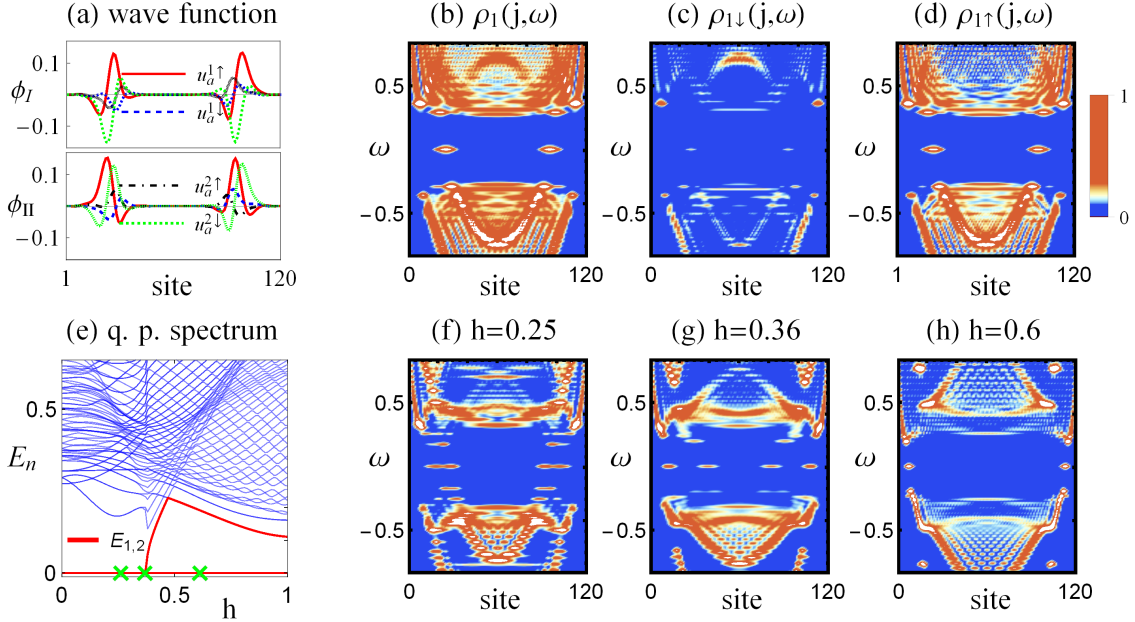


FIG. 10: (a) Wave functions of the MKP related by TR symmetry. (b) LDOS $\rho_1(j, \omega)$ for chain-1. (c) Spin-resolved LDOS $\rho_{1\uparrow}(j, \omega)$. (d) Spin-resolved LDOS $\rho_{1\downarrow}(j, \omega)$. For (a)-(d), $\Omega = 1$. (e) Quasiparticle spectrum versus TR breaking Zeeman field h . (f)-(h) LDOS $\sum_{s=1}^2 \rho_s(j, \omega)$ for three typical h values, as labeled by “cross” in (e). The harmonic trapping potential is $w_x = 0.025$, and other parameter values are the same as those used in Fig. 2(c) in the main text: $\alpha = 1$, $t_{\perp} = 0.5$, and $t = 1$ (set as the energy unit).

The above (hybridized) MKPs can be read out directly from the LDOS (note that $\rho_1(j, \omega) = \rho_2(j, \omega)$ because of the TR symmetry), as illustrated in Fig. 10(b). These zero-energy states localized at the topological boundaries are protected by the pairing gap. For the chain-1, the spin-resolved LDOS is shown in Figs. 10(c)-(d). (For the chain-2, $\rho_{2\uparrow}(j, \omega) = \rho_{1\downarrow}(j, \omega)$ and $\rho_{2\downarrow}(j, \omega) = \rho_{1\uparrow}(j, \omega)$). Our numerics show that these zero-energy states are mainly composed of the spin-up component for the chain-1 and spin-down for the chain-2, indicating the *emergent effective* TR symmetry of the system.

Further, the above LDOS signatures of MKPs are intrinsically different from that of a single Majorana mode. To reveal its double degeneracy, we note that the existence of MKPs are protected by TR symmetry, which would be broken by adding a small Zeeman field $h\sigma_z$ (equal for both chains). In our experimental scheme, the TR-invariant

staggered Zeeman field $\Omega s_z \sigma_z$ is generated by the Hermite-Gaussian beam. The TR-breaking Zeeman field can be easily induced by shifting the system along the y direction. The quasiparticle spectrum is shown in Fig. 10(e). For small h , the lowest quasiparticle excitation is still two-fold degenerate, however the boundary Majorana pair start to separate spatially: one of them moves toward the trap center while the other one moves toward a trap wing slowly [Fig. 10(f)]. At a critical strength $h \approx 0.36$, two Majorana modes coming from the MKPs of different sides collide in the trap center [Fig. 10(g)] and annihilate each other, leaving only one Majorana mode on each wing with further increasing h [Fig. 10(h)].

The above spatial separation of the MKPs in a harmonic trap can be analyzed using the LDA. From the bulk-edge correspondence, the Majorana zero modes should emerge at the boundary between topologically distinct regions, which is determined by the gap closure condition. We start from the uniform system. With an applied Zeeman field (the total Hamiltonian is $\mathcal{H}_k^{\text{BdG}} + h\sigma_z$), the gap closure conditions are given by ($\xi_k = -2t \cos k - \mu$):

$$\xi_k^2 + \Delta^2 + (t_\perp^2 - 4\alpha^2 \sin^2 k^2) - h^2 = \Omega^2, \quad (25)$$

$$\frac{4\alpha^2 \sin^2 k - \Delta^2 + \sqrt{(4\alpha^2 \sin^2 k + \Delta^2)^2 + 4\xi_k^2 h^2}}{2} + h^2 = t_\perp^2. \quad (26)$$

Obviously, in the limit of $h \rightarrow 0$, the above conditions reduce to the TR invariant case (see Eq. (5) in the main text). We locally substitute μ by $\mu(j) = \mu - V(j)$ in the above two equations for the harmonic trap case, from which the positions of the zero modes can be determined. In Fig. 11, we plot the positions of the split Majorana modes as a function of h by numerically solving the gap closure conditions. At $h = 0$, there is one MKP distributed at each side symmetrically. With increasing h , we can find two solutions for each side, corresponding to two split Majorana modes from the same MKP. The numerical solutions agree well with the LDOS pictures shown in Fig. 10(f-h). The splitting becomes faster at larger h , and finally at the critical Zeeman field only one solution survives, consistent with the annihilation of two Majorana modes at the trap center.

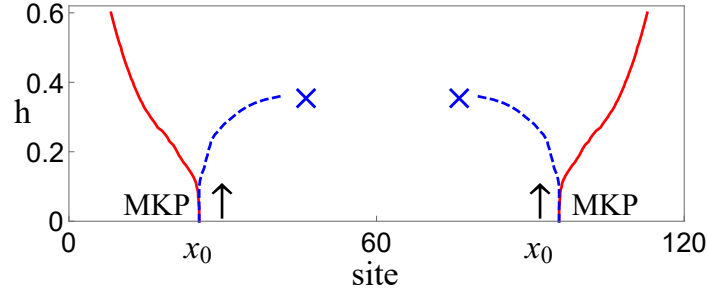


FIG. 11: Spatial splitting of a MKP into two Majorana zero modes in a harmonic trap under a Zeeman field h . The positions of these zero modes (red lines and blue dotted lines) are determined by Eq. (25) and (26) with the parameters from the self-consistent BdG calculations. At $h = 0$, there is one MKP at each side. x_0 denotes the original position of a MKP.

It is worth to mention that, although in general it is hard to write the dependence of μ on h in an explicit form analytically, we can analyze the splitting of the MKP for a small h . Denote the original position of the MKP in a harmonic trap as x_0 . From Eq. (26), we have $4\alpha^2 \sin^2 k = t_\perp^2 - (\xi_k^2 + 1)h^2 + o(h^2)$. Substituting this into Eq. (25), we get $\xi_k^2 = (\Omega^2 - \Delta^2)(1 - h^2) + o(h^2)$, yielding the following relation for the chemical potential:

$$\mu(h) = -2t \cos k - \xi_k = \mu \pm \frac{1}{2} \left[\xi_{k,0} + \frac{t(\xi_{k,0}^2 + 1)}{2\alpha^2} \right] h^2 + o(h^2). \quad (27)$$

Here μ is the chemical potential without adding the Zeeman field, and $\xi_{k,0}^2 = \Omega^2 - \Delta^2$ (Eq. (5) in the main text). Now using the LDA and taking the derivative on both sides of Eq. (27), we can get the following relation:

$$\delta x = \pm \frac{\left[\xi_{k,0} + \frac{t(\xi_{k,0}^2 + 1)}{2\alpha^2} \right] h^2}{4\omega_x^2 x_0}, \quad (28)$$

which determines the shifting of the spatial phase boundary by applying a small Zeeman field. Here the + and - signs correspond to the right- and left-moving zero modes, respectively. The above analysis clearly shows $\delta x \sim h^2$, explaining the slow initial splitting rate of MKP. This point has also been verified directly from our LDOS results.